crystals

MDPI

Article

Thickness-Dependent Thermo-Optical Response in Micro/Nanostructured Bioglass Films

Marco Antonio Hernandez-Acosta [1], Ohtokani Cabrera [2], Ignacio Duarte-Yañez [3], Felipe Gesser Battisti [3,*], Roberto Villarroel [4], Martin Daniel Trejo-Valdez [2] and José Antonio García-Merino [3,*]

[1] Sección de Estudios de Posgrado e Investigación, Escuela Superior de Ingeniería Mecánica y Eléctrica Unidad Zacatenco, Instituto Politécnico Nacional, Mexico City 07738, Mexico; marco.esime@hotmail.com
[2] Escuela Superior de Ingeniería Química e Industrias Extractivas, Instituto Politécnico Nacional, México City 07738, Mexico; ocabrerar1200@alumno.ipn.mx (O.C.); mtrejov@ipn.mx (M.D.T.-V.)
[3] Departamento de Mecánica, Facultad de Ingeniería, Universidad Tecnológica Metropolitana, Jose Pedro Alessandri 1242, Nuñoa, Santiago 7750000, Chile; ignacio.duartey@utem.cl
[4] Departamento de Física, Facultad de Ciencias Naturales, Matemática y del Medio Ambiente, Universidad Tecnológica Metropolitana, Las Palmeras 3360, Ñuñoa, Santiago 7800003, Chile; r.villarroel@utem.cl
* Correspondence: felipegbattisti@utem.cl (F.G.B.); jgarciam@utem.cl (J.A.G.-M.)

Abstract

Bioglass (BG) thin films are promising materials for integrating bioactivity with dynamically tunable optical functionality. Here, BG coatings containing two, four, and six deposited layers were fabricated by spin coating to investigate how deposition-dependent changes in thickness and micro/nanostructural organization relate to the thermo-optical response. Film thicknesses were estimated to be 348, 667, and 1061 nm for BG2, BG4, and BG6, respectively. SEM analysis revealed exposed nanorod-like structures in BG2, whereas increasing the number of layers produced thicker and more consolidated porous architectures. The thermo-optical modulation was experimentally investigated using a cross-polarized transmission setup with a 1064 nm pump beam. All samples displayed comparable photothermal dynamics over the investigated irradiance range. However, their optical modulation showed different temperature dependences, with quadratic trends for BG2 and BG4 and an approximately linear trend for BG6. Differences between optical and thermal dynamics can be associated with nonlinear polarization-sensitive detection, thermal gradients, and thermoelastic or scattering contributions. These results suggest that nanostructured domains, porous morphology, and film–substrate interfaces influence the thermo-optical modulation of BG films. The findings motivate further investigation of these coatings for potential biotechnological photonic applications.

Keywords: Bioglass thin films; thermo-optical modulation; micro/nanostructuring; biointegrated photonics

Check for updates

Academic Editors: Miłosz Grodzicki and Dominika Majchrzak

Received: 11 September 2026
Revised: 2 October 2026
Accepted: 15 October 2026
Published: 16 October 2026

Copyright: © 2026 by the authors. Licensee MDPI, Basel, Switzerland. This article is an open access article distributed under the terms and conditions of the Creative Commons Attribution (CC BY) license.

1. Introduction

Bioglass (BG) materials have attracted considerable scientific and technological interest due to their exceptional bioactivity, biocompatibility, and ability to bond directly with living tissues [1]. Their composition, typically based on 45S5 Bioglass SiO_2–Na_2O–CaO–P_2O_5 systems, promotes the formation of hydroxycarbonate apatite layers when exposed to physiological environments, making them highly suitable for bone regeneration and tissue engineering applications [2,3]. As a result, BG materials have been extensively investigated for orthopedic implants, dental restorations, bone graft substitutes, and bioactive coatings [4–7]. In recent years, advances in thin-film fabrication techniques have enabled the

incorporation of BG coatings onto a wide range of substrates, providing enhanced control over surface chemistry, roughness, porosity, and biological interactions [8,9].

Beyond their well-established biomedical functionality, the structurally tunable architecture of BG thin films enables the integration of biological and photonic functions within a single material platform [10,11]. The effects of BG coatings for potential biointegrated photonics, in which optical signals can be transmitted, detected, or modulated within or in contact with biological tissues, are highly relevant [12]. For example, the degradation of Sm^{3+}-doped 13-93 BG fibers was monitored through luminescence under 405 nm excitation, revealing an almost fivefold difference in degradation rate between fibers containing 0.2 and 2 mol% Sm^{3+} [13]. Nd-containing Ca–Si BG hydrogels also exhibited a linear relationship between fluorescence intensity and local temperature under 808 nm irradiation, allowing 53 °C to be identified as an effective photothermal-treatment temperature [14]. Similarly, Bi-coated BG scaffolds maintained tumor temperatures above 50 °C under 808 nm irradiation and produced approximately 85% tumor necrosis in vivo [15]. These results demonstrate that BG-based materials can support quantitative optical readout and light-activated photothermal functionality. However, these capabilities have largely relied on rare-earth doping or surface modification. This raises the question of whether their micro/nanostructural organization can instead tune the optical response of BG thin films.

One way to evaluate this possibility is to investigate thermo-optical effects, which encompass temperature-induced changes in optical properties and polarization behavior. In homogeneous materials, these responses can involve changes in electronic polarizability and density, thermal expansion, and stress-induced optical anisotropy [16]. In thin films, porosity, interfaces, and thickness can further influence the response, as demonstrated in porous silicon, sol–gel silica films, and TiO_2–Al_2O_3 bilayers [17–19]. In glass ceramics, such as Nd:YAG, laser-induced thermal birefringence generates an orthogonally polarized probe component detectable through a crossed analyzer [20]. Also, temperature dependent optical modulation in Na_2MoO_4:Yb^{3+}, Er^{3+} crystals has also been achieved through upconversion luminescence thermal enhancement, where negative thermal expansion of embedded nanocrystals increases the energy transfer efficiency between lanthanide ions [21]. Similarly, $SrF_2{}^{3+}$ exhibits a temperature-dependent ratio of persistent luminescence intensities governed by the thermal population of coupled Pr^{3+} energy levels, enabling ratiometric thermometry [22]. These findings illustrate that thermal optical responses may involve several mechanisms and depend on both material composition and structural organization. However, the relationship between coating architecture and temperature-dependent optical behavior remains insufficiently explored in BG thin films. Investigating this relationship through cross-polarized transmission measurements can help characterize their optical sensibility to heating and assess their potential for thermally modulated optical coatings.

In this work, layered BG thin films with varying numbers of deposition cycles were fabricated to investigate the relationship between micro/nanostructural evolution and their effective thermo-optical response. Morphological, structural, compositional, and optical characterizations were combined with infrared thermography and polarization-resolved measurements to evaluate temperature-dependent optical modulation induced by localized photothermal excitation. The central objective was to determine whether changes in coating architecture can modify thermo-optical sensitivity independently of the macroscopic temperature evolution. The results demonstrate that BG coatings with comparable heating and cooling behavior exhibit different thermo-optical sensitivities, thereby supporting a relationship between optical modulation and micro/nanostructural organization.

2. Materials and Methods

2.1. Bioglass Synthesis

BG powders with a nominal composition of SiO_2–Na_2O–CaO–P_2O_5 were synthesized through a modified sol–gel route. Initially, a hydrolysis solution was prepared by mixing 11.2 mL of deionized water, 0.5 mL of HCl, and 2.17 mL of ethanol under continuous magnetic stirring. Subsequently, 26.21 mL of tetraethyl orthosilicate (TEOS, Sigma-Aldrich, St. Louis, MO, USA) and 0.63 mL of triethyl phosphate (TEP, Sigma-Aldrich, St. Louis, MO, USA) were added as silica and phosphorus precursors, respectively. In a separate container, 10.95 g of calcium nitrate [$Ca(NO_3)_2$] (Sigma-Aldrich, St. Louis, MO, USA) and 5.66 g of sodium chloride (NaCl,) (Sigma-Aldrich, St. Louis, MO, USA) were dissolved in 20 mL of deionized water under magnetic agitation. After complete dissolution, this solution was gradually incorporated into the TEOS/TEP mixture and stirred continuously for 3 h to promote hydrolysis and polycondensation reactions. The resulting sol was allowed to gel and subsequently subjected to a multistep thermal treatment. The gel was first heated at 200 °C to remove residual solvents and organic species, followed by a second thermal stage at 450 °C to promote structural consolidation. Finally, the material was calcined at 650 °C to promote structural stabilization and remove remaining nitrates and chloride-derived species. The obtained BG powder was then mechanically ground and used as the precursor material for thin-film fabrication.

2.2. Thin Films Deposition

BG thin films were deposited onto square silica substrates (1.2 × 1.2 cm with roughly 1 mm thickness). Prior to deposition, the substrates were rinsed with distilled water and subsequently cleaned in an ultrasonic bath with acetone for 25 minutes to remove residual contaminants and organic impurities. The coatings were fabricated using the spin-coating technique, and the BG powder was dispersed in ethanol and homogenized under magnetic stirring prior to deposition. For each deposition cycle, 70 µL of suspension was dispensed onto the substrate surface and uniformly distributed by rotation. Multiple-layer films were prepared by performing sequential deposition cycles, with the samples divided into three groups of 2, 4, and 6 coating layers, respectively. To promote solvent evaporation and structural stabilization, an intermediate thermal treatment at 240 °C was applied after each deposition step. This heating stage ensured gradual densification and improved adhesion of the deposited layers before the subsequent coating cycle. Finally, three sample stages were obtained as a function of layer deposition: BG2, BG4, and BG6 for 2, 4, and 6 coating layers, respectively.

2.3. Characterization

The morphological and compositional characterization of the materials involved in the present work was performed using field-emission scanning electron microscopy (FESEM) and energy-dispersive X-ray spectroscopy (EDS), respectively. The equipment was a GeminiSEM 360 FESEM (ZEISS, Wetzlar, Germany). The samples were sputter-coated with chrome before SEM analysis. EDS measurements were performed at an accelerating voltage of 5 kV to reduce the electron interaction volume and minimize the contribution from the silica substrate. SEM images were processed in MATLAB (R2023b) to delineate the contours of prominent cracks and surface voids through grayscale-based segmentation. The segmented area fraction was calculated as the ratio of selected pixels to the total analyzed image area. Structural analysis was performed using Raman spectroscopy (Witec alpha 300 RA system, Ulm, Germany) with a 532 nm wavelength laser excitation. A Raman spectrum of the bare silica substrate was independently acquired under the same experimental conditions and used to subtract the substrate contribution from the BG spectra prior to

spectral deconvolution and calculation of the relative Raman-band intensities. Finally, the optical properties were measured in a UV–Vis range in transmittance mode using a spectrophotometer (model HR-2XR200-25, Ocean Optics, Dunedin, FL, USA).

2.4. Photothermal Effects

The photothermal response of the BG films was evaluated using the optical arrangement shown in Figure 1. A near-infrared (NIR) laser at 1064 nm wavelength with nanosecond pulse irradiation (25 ns pulse duration, and ~11 μJ per pulse) was employed as the pump source to induce localized heating in the sample. The average power laser was modulated by changing the pulse repetition rate from 2 to 20 kHz, and was varied from 22 to 228 mW. Additionally, a laser probe beam at 520 nm (Thorlabs NPL52B, with 4 mW of power, and 1 MHz repetition rate) was used to monitor thermally induced optical changes. Both beams were focused onto the same region of the sample surface using plano-convex lenses (f = 150 mm, beam waist diameter ~300 μm) and aligned to propagate through the film at a 26° incidence angle. With these values the mean pump irradiance was computed between 31 W/cm^2 to 322 W/cm^2. The probe and pump beams were vertically polarized using linear polarizers. After transmission, the probe beam was collected by a condenser and focused onto a second polarizer (analyzer) oriented orthogonal to the incident polarization state. This crossed-polarizer configuration enabled the detection of thermally induced polarization changes generated in the BG films. The transmitted optical power was measured using a Newport 818-SL/DB photodetector (Newport Corporation, Irvine, CA, USA) connected to a Newport 843-R optical power meter interface. Since the sample exhibits scatter, a low-pass optical filter was placed before the detector to suppress residual pump radiation and ensure selective detection of the probe beam.

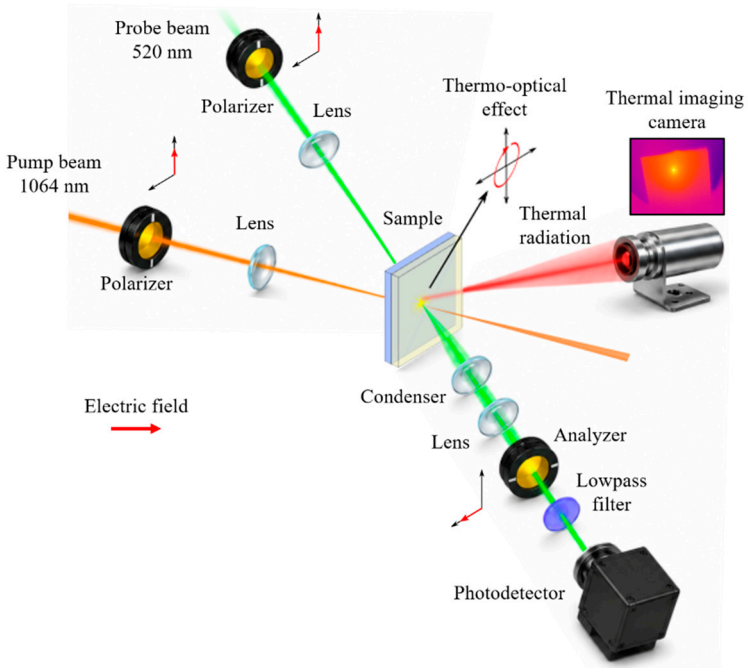


Figure 1. Photothermal experimental diagram.

Simultaneously, the surface temperature distribution was monitored using an Optris Xi 400 infrared camera, featuring a spatial resolution of 80 μm per pixel and a temperature measurement accuracy of ±2%. The thermal images were recorded throughout the laser excitation process to determine the temporal evolution of the temperature increase induced by the pump beam. Photothermal excitation produces local temperature gradients in the BG-coated substrates and may modify the polarization and scattering of the probe beam.

The resulting optical response was monitored using a crossed-polarizer configuration and quantified as the change in normalized transmission:

$$\Delta C_{\perp}(T) = \frac{P_{\perp}(T) - P_{\perp}(T_0)}{P_{\parallel}(T_0)} \quad (1)$$

where T is the temperature, T_0 is the initial temperature, $P_{\perp}$ is the orthogonal transmitted optical power, and $P_{\parallel}$ is the maximum probe power measured with the analyzer parallel to the input polarizer before heating. This quantity describes the change in the detected cross-polarized signal and does not independently determine birefringence or refractive-index variation. Finally, the optical modulation sensitivity was evaluated from the fitted dependence of $\Delta C_{\perp}$ on ΔT.

3. Results

Figure 2 presents SEM micrographs of the BG thin films prepared with different numbers of deposition layers. Far-view images (Figure 2a,c,e) reveal an evolution of the surface morphology as the number of deposited layers increases. BG2 (Figure 2a) exhibits a discontinuous surface composed of interconnected islands separated by large voids and microcracks, indicating incomplete surface coverage. In BG4 (Figure 2c), connectivity between neighboring regions increases, and uncovered areas become smaller, resulting in a more homogeneous porous network. Finally, in Figure 2e, sample BG6 exhibits a continuous, highly interconnected microstructure with a dense distribution of pores across the entire surface. To complement the qualitative SEM observations, prominent cracks and surface voids were segmented in the analyzed fields (Figure S1). The segmented area fractions were 4.04%, 5.77%, and 9.81% for BG2, BG4, and BG6, respectively. BG2 shows localized openings and cracks, whereas BG6 exhibits a more distributed pattern of smaller void-like features alongside larger cracks. These values provide a quantitative descriptor of the visible surface morphology rather than a measure of volumetric porosity. Additionally, the high-magnification images (Figure 2b,d,f) provide further insight into the nanoscale structure of the coatings. Figure 2b shows that sample BG2 has a well-defined texture composed of nanorods-like features distributed throughout the surface. Similar features remain observable in the BG4 sample, as shown in Figure 2d, although with reduced definition due to the increasing consolidation of the coating. In contrast, nanostructuring is less distinguishable when the number of layers increases to 6. In the BG6 sample, as shown in Figure 2f, the surface evolves toward a smoother and more compact appearance. These observations suggest a progressive morphological transition from surface-exposed nanostructured features to a more uniform and interconnected porous microstructure as the number of deposition cycles increases. The reduced visibility of these surface features should therefore be interpreted as a morphological change rather than as evidence of altered structural composition.

Moreover, the cross-sectional SEM micrographs of the BG are shown in Figure 3. The mean film thickness were 348 nm (Figure 3a), 667 nm (Figure 3b), and 1061 nm for BG2, BG4, and BG6, respectively. The increase in thickness confirms the progressive accumulation of material during the sequential spin-coating process. In addition to the thickness growth, morphological changes are also evident in the cross-sectional images. BG2 exhibits a relatively thin and compact layer with a well-defined interface with the substrate, whereas BG4 and BG6 develop increasingly rough surfaces and a more complex porous architecture.

Additionally, the elemental composition of the BG coatings was evaluated by EDS at an accelerating voltage of 5 kV, and the results are summarized in Table 1. Signals corresponding to O, Si, Na, Ca, and P were detected in all samples, confirming the presence of the nominal constituent elements of the BG system after the deposition and thermal

treatment [23]. The relatively low accelerating voltage was selected to reduce the electron interaction volume and minimize substrate contribution. Nevertheless, because the coatings are porous and their thickness ranges from approximately 0.35 to 1.06 µm, contribution from the SiO_2 substrate cannot be completely excluded, particularly for BG2. In addition, quantitative EDS analysis at 5 kV presents limitations for some elements, particularly Ca. Therefore, the values reported in Table 1 should be considered semi-quantitative and are not used here to establish the absolute stoichiometry of the BG coatings.

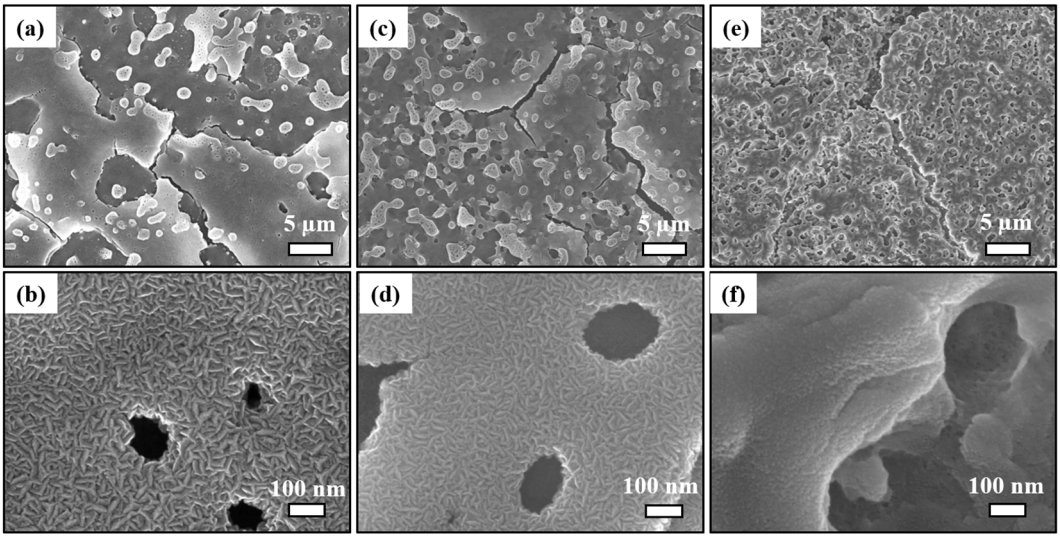


Figure 2. SEM surface analysis of BG thin film with different layer deposition. (**a**,**b**) BG2, (**c**,**d**) BG4, and (**e**,**f**) BG6.

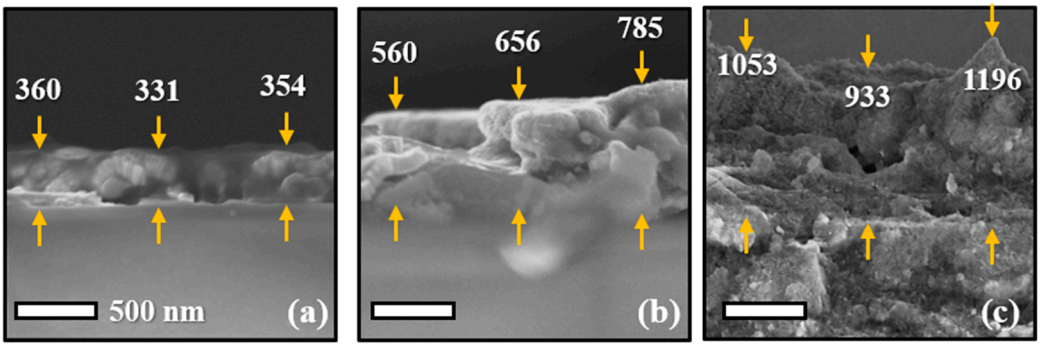


Figure 3. SEM micrograph of the lateral view of the BG thin film with different layer deposition. (**a**) BG2, (**b**) BG4, and (**c**) BG6.

Table 1. Semi-quantitative EDS analysis of BG samples as a function of deposition layers.

Element	Content (%wt)		
	BG2	BG4	BG6
O	58.9	55.2	60.8
Si	24.1	28.8	25.7
Na	8.6	9.1	5.3
Ca	5.5	3.3	4.1
C	2.7	3.1	3.9
P	0.2	0.5	0.2

Figure 4 shows the Raman spectra of the BG coatings and the bare silica substrate. As the film thickness decreases, the substrate contribution becomes increasingly prominent

because of the smaller scattering volume of the coating. Consequently, the BG2 spectrum exhibits a strong overlap with the silica substrate, while the characteristic BG bands become more evident for BG4 and BG6. The main BG-related bands are located at approximately 956 and 1045 cm^{-1}, within the spectral region associated with silicate-network vibrations and possible phosphate contributions [24]. After deconvolution of the Raman spectra and subtraction of the substrate contribution, the intensity ratios I_{956}/I_{1045} were found to be 0.12, 0.17, and 0.14 for BG2, BG4, and BG6, respectively. Although small differences are observed, the ratio does not exhibit a systematic dependence on the number of deposited layers. Therefore, within the sensitivity of the Raman measurements and considering the substrate contribution, no substantial layer-dependent variation in the relative populations can be established. Raman spectroscopy alone cannot exclude subtle structural evolution or the presence of minor crystalline phases.

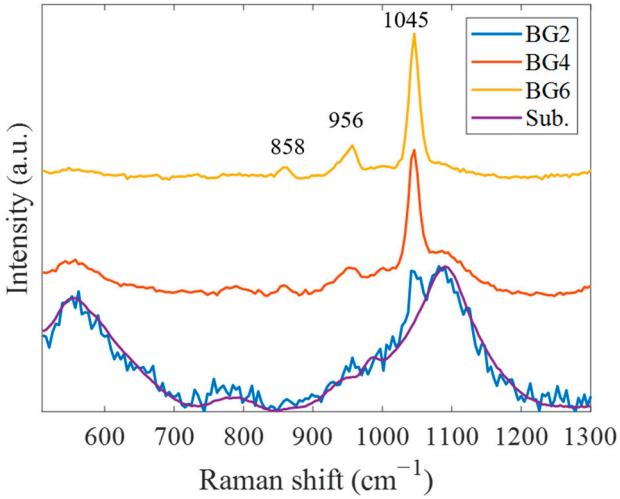


Figure 4. Raman spectra of BG samples.

Figure 5 shows the measured transmittance spectra of the bare SiO_2 substrate and the BG-coated substrates. Over the 400–1000 nm measurement range, the bare substrate exhibits the highest transmittance. Among the coated samples, transmittance follows the order BG2 > BG4 > BG6 and generally increases toward longer wavelengths. This behavior is consistent with the increasing amount of deposited material from BG2 to BG6. Empirical exponential fits to the coated-sample spectra were used to estimate the transmittance at the 1064 nm pump wavelength, yielding 69.0% for BG2, 64.7% for BG4, and 52.6% for BG6. These extrapolated values provide estimates of the transmittance at the pump wavelength and help contextualize the samples' photothermal response. The coefficients of determination of the three fittings were computed in $R^2 > 0.999$.

Figure 6 shows the photothermal map in the BG samples as a function of five characteristic times (0, 10, 20, 30, and 40 s), where (t = 0 s) corresponds to the onset of laser irradiation at 158 mW. The infrared thermographic images provide a 2D visualization of the spatial temperature distribution generated by optical excitation and reveal the progressive formation of a localized thermal gradient centered at the beam impact region. As the irradiation time increases, the thermal spot expands radially while maintaining a nearly symmetric temperature profile, indicating homogeneous heat diffusion from the excitation area toward the surrounding regions. No evidence of preferential heat propagation paths, thermal discontinuities, or localized hot spots associated with structural defects is observed, suggesting uniform thermal coupling between the BG coatings and the substrate. Furthermore, despite the differences in optical transmittance among BG2, BG4, and BG6, the thermographic maps exhibit comparable spatial temperature distributions and heating

dynamics. To further explore this effect, spatial and transient analyses were conducted in the samples.

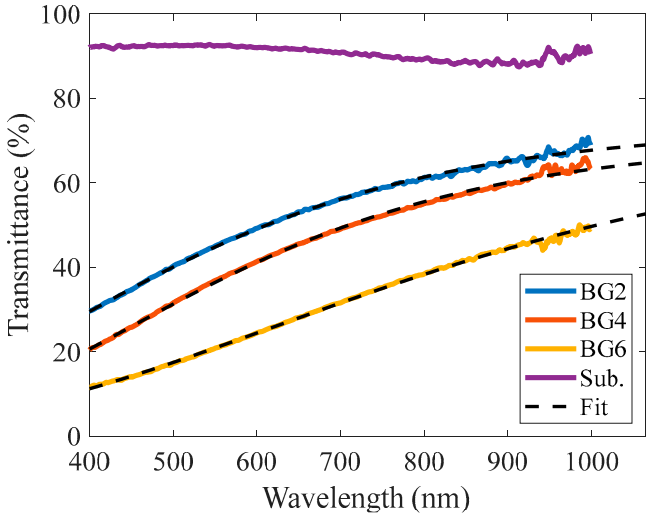


Figure 5. UV–Vis transmittance of bare SiO_2 and BG-coated substrates. Solid lines are measured spectra; dashed lines are exponential fits extrapolated to 1064 nm.

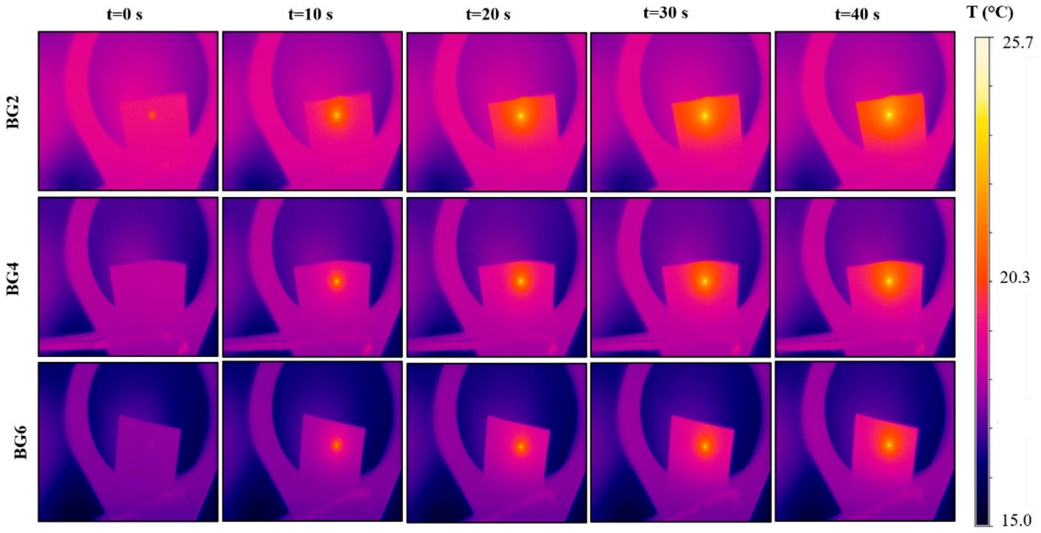


Figure 6. Spatial and transient photothermal evolution thermography of the 3 studied samples at 158 mW of laser power.

Figure 7 presents the temperature profiles extracted along the x direction across the irradiated region for BG2, BG4, and BG6 at different evolution times based on the results of Figure 6. The profiles reveal the progressive formation of a localized thermal gradient centered at the excitation region, followed by a gradual spatial decay as heat diffuses toward the surrounding areas. Remarkably, all samples exhibit nearly identical spatial temperature distributions and temporal evolution throughout the experiment, despite the differences observed in their optical transmittance. This behavior suggests that the photothermal response is predominantly governed by the thermal properties of the silica substrate rather than by the BG coatings themselves. Consequently, the deposited layers do not significantly alter the overall heat generation or diffusion process under the experimental conditions employed.

The substrate's thermal diffusivity, $\alpha \approx 6\text{–}10 \cdot 10^{-7}$ m^2/s [25] (fused silica), allows rationalizing this behavior. Axial (through the substrate thickness) heat diffusion is orders of magnitude faster than the tens-of-seconds time scale of the experiment, whereas radial

(in-plane) heat diffusion cannot be similarly ruled out since it occurs on a comparable timescale (see Appendix A). The transient behavior may involve both lateral heat diffusion and heat exchange with the surroundings. As detailed in Appendix A, this behavior is consistent with the photothermal dynamics being independent of sample thickness.

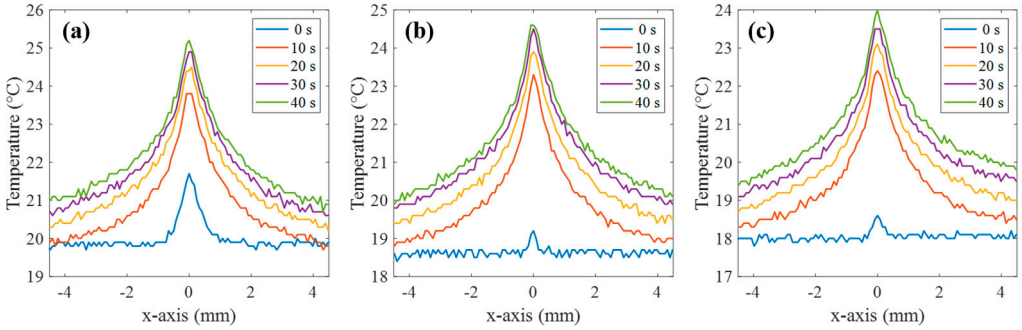


Figure 7. Photothermal profile in line of the beam as a function of time and layer deposition. (**a**) BG2, (**b**) BG4, and (**c**) BG6.

To study the transient photothermal behavior in depth, the samples were evaluated across three characteristic regions, as illustrated in Figure 8a. All measurements were acquired at a laser power of 158 mW, as shown in Figure 1. Area 1 (A1) corresponds to the maximum temperature reached at the laser spot, A2 represents the mean temperature in the vicinity of the irradiated region, and A3 monitors the temperature evolution at a distant location from the excitation source. These regions provide complementary information regarding heat generation and propagation, including the maximum heating rate (A1), the average thermal response near the irradiated zone (A2), and an indirect assessment of lateral heat diffusion across the surface (A3). The temporal evolutions for each zone are presented in Figure 8b and 8c, and 8d, for BG2, BG4, and BG6 samples, respectively. The transient photothermal effect in the samples exhibits similar behavior in the heating and cooling stages. Additionally, Figure 8e–g show the temporal evolution of the samples and substrate in each evaluation area. It is observed that, during the heating stage in the irradiated zone, all samples exhibited a rapid temperature increase followed by a gradual approach to a quasi-steady state. Remarkably, the heating and cooling dynamics were highly similar across all samples, with the substrate showing slightly less similarity in all analyzed regions. These results indicate that the thermal response under laser irradiation remains similar among all investigated samples, despite the differences in coating thickness. Such behavior indicates that the overall photothermal evolution is primarily governed by the SiO_2 substrate, which dominates thermal storage and diffusion under the experimental conditions employed.

On the other hand, Figure 9 summarizes the thermo-optical response of BG films. Figure 9a shows the cross-polarized transmission ($\Delta C_\perp$) as a function of the induced change in temperature (ΔT), computed using Equation (1). The pump power was varied from 22 to 228 mW, producing similar temperature increases among the coatings, as shown in the inset. BG2 and BG4 exhibited a quadratic dependence, whereas BG6 showed an approximately linear response and the largest signal over most of the measured range. The substantially smaller response of the bare SiO_2 substrate indicates that the coatings contribute to the observed optical modulation. The data were fitted using $\Delta C_\perp = a(\Delta T)^2 + b\Delta T$, and Table 2 reports the coefficients as estimate $\pm$ one standard error, together with the corresponding determination coefficient (R^2) values. All thermographic measurements used $\varepsilon = 1$; an assumed emissivity range of 0.8–1.0 [26] yielded an estimated temperature difference of approximately 0.7 °C near 25 °C under the conditions considered, which was included as an additional contribution to the horizontal error bars. This estimate accounts for possible

emissivity effects without providing a sample-specific correction. Figure S2 presents both horizontal and vertical error bars, with the latter representing the photodetector resolution of ±5 nW normalized by the initial maximum parallel transmitted power.

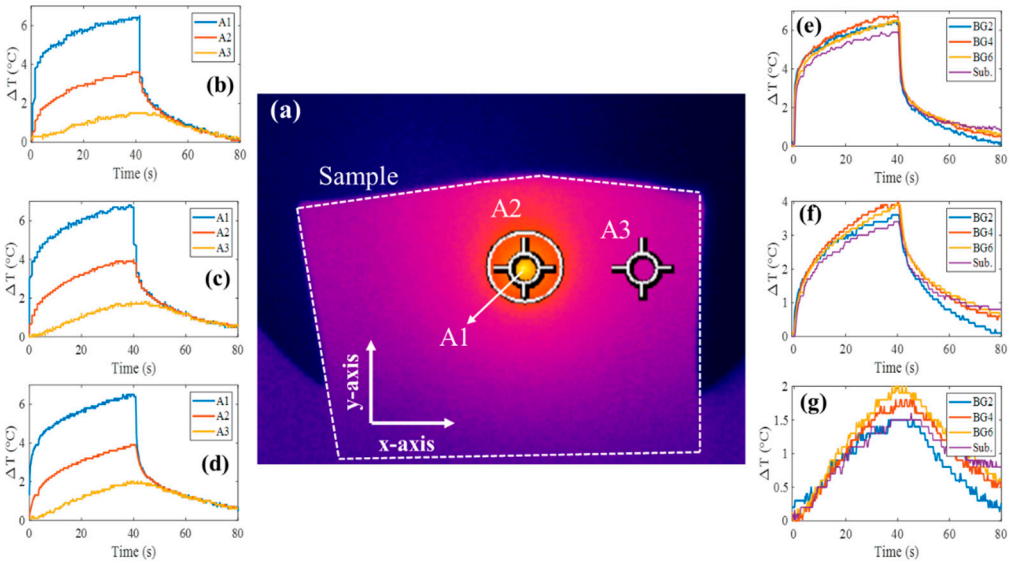


Figure 8. (**a**) Photothermal areas consideration for transient evaluations; (**b**) BG2; (**c**) BG4; (**d**) BG6; (**e**) A1; (**f**) A2; and (**g**) A3.

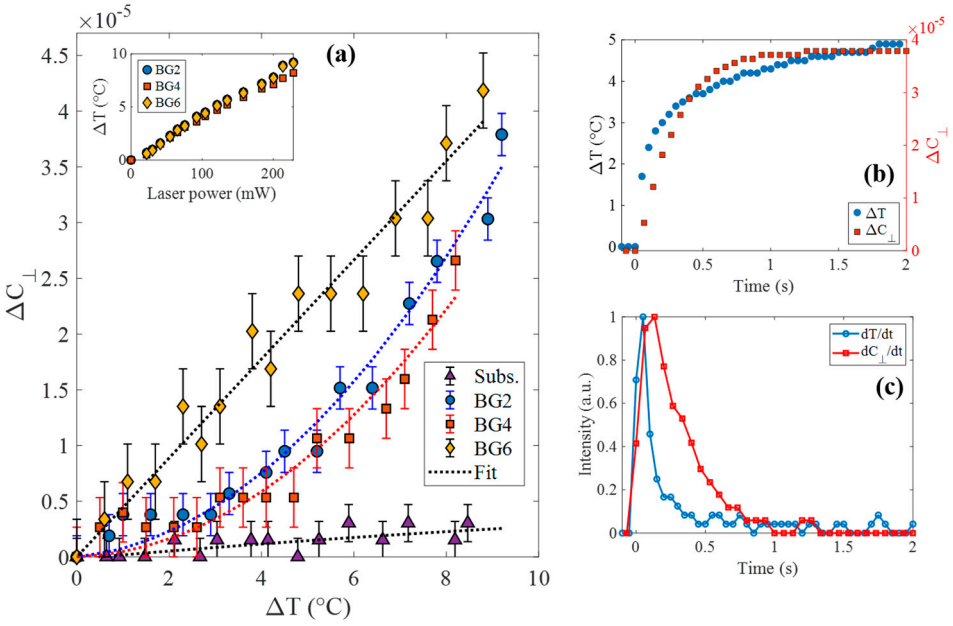


Figure 9. Thermo-optical response of BG samples. (**a**) $\Delta C_{\perp}$ vs ΔT (inset: ΔT as a function of pump laser power). (**b**) Transient behavior of thermal and optical signals in the BG2 sample. (**c**) Normalized time derivatives of the thermal and optical signals.

Table 2. Fitting coefficients for $\Delta C_{\perp}$ versus ΔT, reported as estimate ± one standard error, and corresponding R^2 values.

Sample	Fitting Coefficients		
	$a \times 10^{-7}$ (°C^{-2})	$b \times 10^{-7}$ (°C^{-1})	R^2
BG2	3.7 ± 0.45	4.01 ± 3.3	0.9755
BG4	3.28 ± 0.63	1.53 ± 1.15	0.933
BG6	-	44.4 ± 1.13	0.9656

To further investigate the origin of the optical response, the temporal evolution of ΔT and $\Delta C_{\perp}$ was analyzed simultaneously, as shown in Figure 9b. Both exhibited similar heating trends, although the optical response showed a slight initial delay and approached its plateau earlier. Moreover, Figure 9c compares the normalized time derivatives of the temperature and cross-polarized transmission signals. The optical derivative exhibits a more prolonged decay, which may reflect the nonlinear dependence of the optical signal on temperature. Spatial thermal gradients, thermoelastic stress, and changes in scattering may also contribute, since thermography measures surface temperature whereas the optical signal integrates contributions across the probe beam and the film–substrate system interphase [27,28]. These observations alone do not establish a distinct thermoelastic relaxation process.

4. Discussion

The central finding of this study is that BG-coated samples exhibit a temperature-dependent change in cross-polarized probe transmission whose functional dependence varies with the number of deposited layers, despite their comparable photothermal behavior. As shown in Figure 9a, BG2 and BG4 exhibit a quadratic dependence on temperature change, whereas BG6 displays an approximately linear response. These differences should be considered alongside the deposition-dependent evolution of the coatings. Within the limitations of substrate contributions and measurement sensitivity, EDS and Raman analyses revealed no systematic layer-dependent compositional or vibrational changes. In contrast, SEM showed a clear morphological evolution from the discontinuous, island-like coating with exposed nanorod-like features in BG2 to the more continuous and interconnected porous architecture of BG6. The reduced visibility of the nanoscale features with increasing deposition cycles may reflect progressive coverage and consolidation of the outer layers. Previous studies have shown that morphology and void fraction can substantially modify the effective optical properties of thin films [29,30]. For example, at 2 μm, the transformation of dense Ir films into branched structures with a larger void fraction reduced the refractive index from approximately 4.2 to 2.4 and the extinction coefficient from 12 to 2.3 [30]. Although this metallic system is not quantitatively comparable with BG, it demonstrates that structural organization can substantially modify effective optical constants without changing the nominal film material. Moreover, studies of nanoporous films highlight the influence of morphology and polarization on optical propagation and the need to consider scattering when interpreting effective optical losses [31]. These findings provide a basis for considering microstructural contributions to the observed cross-polarized signal, although the present measurements do not isolate their role from other thermally induced effects in the film–substrate system.

Table 3 summarizes evidence that porosity, thickness, and interfaces influence temperature-dependent optical properties [17–19], while pore structure can also affect scattering and polarization [27]. These effects provide possible explanations for the different optical responses observed here despite comparable heating. Thermal expansion mismatch between the BG coating and the silica substrate, together with spatial thermal gradients, may generate nonuniform stresses and photoelastic changes [32]. Pores, cracks, and differences in coating connectivity may modify local stiffness and stress redistribution, thereby affecting the polarization response to a given temperature change. The quadratic response of BG2 and BG4 may arise from crossed-polarizer detection, which near extinction converts a phase retardation proportional to ΔT into an intensity change proportional to $(\Delta T)^2$. The approximately linear response of BG6 could instead reflect a different initial retardation or a greater contribution from temperature-dependent scattering and depolarization, although these possibilities cannot be distinguished with the present measurements. These mechanisms also help interpret Figure 9c. A nonlinear dependence of the optical signal on

temperature can modify its time derivative even without an independent relaxation process, while evolving thermal gradients and stresses may further affect the signal integrated over the probe region. Thus, the differences between the optical and thermal derivatives are consistent with a combination of polarization-sensitive detection, spatially distributed heating, and possible thermoelastic contributions, rather than conclusive evidence of a separate slow process.

Table 3. Structure-dependent thermo-optical responses in porous and thin-film systems.

Material System	Structural Variation	Main Finding	Measurement Method
Porous Si [19]	Different porosities	Thermo-optic coefficient decreases with porosity and depends on wavelength.	Temperature-dependent optical measurements.
Porous SiO_2 [18]	Porous film structure and different film thicknesses	Negative thermo-optic coefficients and distinct temperature regimes were observed, with partially reversible refractive-index changes upon cooling.	Temperature-dependent spectroscopic ellipsometry
TiO_2–Al_2O_3 bilayer [17]	Al_2O_3 barrier-layer thickness varied over a fixed TiO_2 layer	Barrier-layer thickness modifies the temperature dependence of the refractive index and can change the sign of the thermo-optic coefficient.	Temperature-controlled spectroscopic ellipsometry
Macroporous SiO_2 films [27]	Large range of porosity, and inorganic versus hybrid composition	Pore structure influences the degree of polarization through multiple scattering and structural anisotropy.	Polarization-resolved speckle imaging, and Stokes-parameter analysis.
BG films on SiO_2 substrates (this work)	Number of deposited layers and changes in thickness and surface morphology	Cross-polarized transmission increases with temperature, showing quadratic trends for BG2/BG4 and an approximately linear trend for BG6.	Crossed-polarizer pump–probe setup.

These possible microstructural contributions are also consistent with the absence of a simple proportional relationship between coating thickness and optical modulation. Although BG6 exhibits the largest $\Delta C_{\perp}$ over most of the measured range, the signals become comparable at the highest temperature changes studied, despite the approximately threefold difference in thickness between BG2 and BG6. Together with their different temperature dependences, this behavior suggests that thickness alone does not determine the observed modulation and that deposition-dependent changes in morphology, connectivity, and interfaces may also contribute. For BG2, the discontinuous surface coverage further limits the use of the local cross-sectional thickness as a measure of the amount of material sampled by the probe. The present results therefore demonstrate that a thinner coating can produce a comparable normalized optical signal under specific thermal conditions, but they do not establish the extent of the optically active region or the modulation efficiency per unit of material.

From an application perspective, excitation at 1064 nm is relevant because this wavelength has been used to remotely activate bone-regeneration scaffolds. For example, 1064 nm irradiation of a CuS–PEG–PCL scaffold enabled controlled dexamethasone release

and mild heating at 42 ± 0.5 °C, promoting osteogenic differentiation [33]. Although this system did not contain BG, it demonstrates the feasibility of using NIR light to activate functional materials designed for bone repair. In BG-based systems, photothermal activation and bone-tissue regeneration have also been combined using Bi-doped phosphosilicate glasses under 808 nm irradiation [34]. In the present work, NIR irradiation produced a measurable, temperature-correlated change in the cross-polarized probe transmission of the BG-coated samples. However, waveguiding, self-focusing, biological sensing, and therapeutic performance were not evaluated. These functions require dedicated optical, biological, and in vivo studies before the coatings can be considered for biointegrated applications.

5. Conclusions

BG thin films exhibited a clear morphological evolution from exposed nanorod-like features in BG2 to a thicker, more consolidated porous architecture in BG6. EDS and Raman measurements revealed no systematic trends in elemental composition or relative Raman-band intensities within the limitations of these analyses. Under 1064 nm excitation, the coatings showed comparable photothermal dynamics, but distinct temperature-dependent changes in cross-polarized probe transmission. BG2 and BG4 exhibited quadratic trends, whereas BG6 showed an approximately linear response and the largest signal over most of the measured range. The smaller response of bare SiO_2 indicates that the coatings contribute to the optical modulation. Moreover, the optical signal did not increase proportionally with coating thickness, suggesting that morphology and interfaces also influence the response. Differences between the thermal and optical time derivatives may reflect nonlinear polarization-sensitive detection, thermal gradients, and possible thermoelastic or scattering effects linked to the coating's micro/nanostructure. Although these contributions were not independently resolved, the findings demonstrate temperature-dependent optical modulation in BG-coated substrates and motivate further research into their potential use in light-controlled biotechnological applications.

Supplementary Materials: The following supporting information can be downloaded at: https://www.mdpi.com/article/10.3390/cryst16100668/s1, Figure S1: Image processing analysis of SEM micrographs of segmented cracks and prominent surface voids highlighted in red. (a) BG2, (b) BG4 and (c) BG6. Scale bar 5 µm. The segmented area fractions are 4.04%, 5.77%, and 9.81%, respectively; Figure S2: Normalized change in cross-polarized transmission, AC1, as a function of temperature change, ΔT: (a) comparison of BG2, BG4, BG6, and the bare silica substrate; (b–d) individual data for BG2, BG4, and BG6, respectively. Horizontal error bars include the estimated temperature uncertainty associated with an assumed emissivity range of 0.8–1.0.

Author Contributions: Conceptualization, O.C., M.D.T.-V. and J.A.G.-M.; Methodology, M.A.H.-A., R.V. and J.A.G.-M.; Software, I.D.-Y. and J.A.G.-M.; Validation, I.D.-Y., F.G.B. and J.A.G.-M.; Formal analysis, J.A.G.-M.; Investigation, M.A.H.-A., O.C., R.V. and J.A.G.-M.; Resources, M.D.T.-V.; Data curation, M.A.H.-A., F.G.B. and R.V.; Writing—original draft, I.D.-Y. and J.A.G.-M.; Writing—review and editing, F.G.B. and J.A.G.-M.; Visualization, J.A.G.-M.; Project administration, R.V. and M.D.T.-V. All authors have read and agreed to the published version of the manuscript.

Funding: This research was funded by Agencia Nacional de Investigación y Desarrollo grant number 11250606; Agencia Nacional de Investigación y Desarrollo grant number 11251840; Agencia Nacional de Investigación y Desarrollo grant number 85220101 and Metropolitan University of Technology grant number LE24-01.

Data Availability Statement: No new data were created or analyzed in this study. Data sharing is not applicable to this article.

Acknowledgments: The authors thank ANID for FONDECYT Iniciación projects N°11250606 (JAGM), N°11251840 (RV), and Project Subvención a la Instalación en la Academia, convocatoria 2022,

N°85220101, and FE-SEM equipment UTEM (MINEDUC-UTM 1999) for partial financial support. Also, we kindly acknowledge: The Project supported by the Fund for Scientific and Technological Equipment, year 2024, code LE24-01, Universidad Tecnológica Metropolitana. UTEM, Santiago, CHILE. During the preparation of this work, the authors used ChatGPT-6/Gemini-3.1/Claude-5.5/Grammarly- v.1.2.300.1965 to improve the English language and to refine Figure 1. After using this tool/service, the authors reviewed and edited the content as needed and took full responsibility for the content of the published article.

Conflicts of Interest: The authors declare that there are no conflicts of interest.

Appendix A

Thermal-Diffusion Analysis

Based on the pump-beam spot size ($\omega \approx 300 \cdot 10^{-6}$ m), the substrate thickness ($L_{sub} \approx 1 \cdot 10^{-3}$ m), and the substrate's thermal diffusivity (in the range $\alpha \approx 6$–$10 \cdot 10^{-7}$ m^2/s for fused silica), this appendix (i) develops an order-of-magnitude argument indicating that axial heat diffusion is not the source of the tens-of-seconds transient observed, while radial heat diffusion occurs on a comparable timescale and cannot be excluded and (ii) evaluates the external thermal boundary condition (lumped heat exchange with the surroundings) as the contributing mechanism.

Regarding the radial heat diffusion, the instantaneous, free-space Green's function for the heat equation in n dimensions is an isotropic Gaussian, i.e., $T \propto (4\pi\alpha t)^{-\frac{n}{2}} \exp\left(-\frac{r^2}{4\alpha t}\right)$ [35], whose mean-square spreading obeys $\langle r^2 \rangle = 2n\alpha t$ [36]. For radial (in-plane) spreading, this is a $2D$ problem (i.e., $n = 2$), giving the characteristic time to spread across $r = \omega/2$ as:

$$t_r \sim \frac{(\omega/2)^2}{4\alpha} \rightarrow t_r \sim 5.6\text{–}9.4 \cdot 10^{-3} \text{ s}. \tag{A1}$$

This form is appropriate because radial heat diffusion is effectively unbounded, since the substrate's in-plane dimensions are $1.2 \times 1.2 \cdot 10^{-2}$ m, far larger than the pump spot ω, and such an approximation is appropriate at the timescale shown.

Next, it is necessary to evaluate if the radial diffusion reaches the substrate's lateral extent within the observed transient. Using the relevant length $L \approx 6 \cdot 10^{-3}$ m (half the plate width) in place of $\omega/2$:

$$t_L \sim \frac{L^2}{4\alpha} \rightarrow t_L \sim 9.0\text{–}15.0 \text{ s}. \tag{A2}$$

This is the same order of magnitude as the observed 20–40 s transient. The radial Fourier number $Fo = \alpha t/L^2$ at the observed times ranges from 0.33 to 1.11, i.e., order unity, therefore radial (in-plane) conduction to the finite substrate boundary cannot be ruled out as a contributor to the observed timescale.

The axial direction is a physically different problem since the substrate has a real boundary at depth L_{sub}, so the relevant classical solution is not free-space spreading, but instead a $1D$ heat diffusion into a semi-infinite solid. The surface temperature response following step heating or constant heat flux takes the functional form of the complementary error function, $\mathrm{erfc}\left(\frac{z}{2\sqrt{\alpha t}}\right)$ [35], from which the thermal penetration depth follows as $\delta(t) = 2\sqrt{\alpha t}$ [37]. When $\delta(t) < L_{sub}$, the substrate acts as an infinitely thick medium because the thermal front has not reached the back boundary. The crossover to finite-thickness behavior occurs when the thermal front reaches the back of the substrate, i.e., $\delta(t_z) = L_{sub}$, so [38]:

$$t_z \sim \frac{L_{sub}^2}{4\alpha} \rightarrow t_z \sim 2.5\text{–}4.2 \cdot 10^{-1} \text{ s} \tag{A3}$$

At $t > t_z$, the substrate is thermally saturated; hence, this semi-infinite solution is valid for $t \ll t_z$, and it does not describe the substrate's behavior during the actual 20–40 s observation window.

Again, the Fourier number $Fo_z = \alpha t / L_{sub}^2$ determines which regime applies at the observed timescale. In this case, Fo_z(20–40 s) ≈ 12–40 ≫ 1, so the substrate is thermally saturated (i.e., uniform temperature through its full thickness) well before the observed plateau. Then, one should read t_z as a crossover time beyond which the semi-infinite picture breaks down, not as the axial diffusion time during the measurement. This estimate shows that diffusion across the substrate thickness occurs much faster than the observed transient, whereas lateral diffusion remains relevant on the experimental timescale.

Axial heat diffusion has been ruled out as the source of the transient observed, but radial conduction occurs on a comparable timescale to the observed transient (Fo_r ~ 0.3–1.1) and cannot be similarly excluded. The tens-of-seconds transient likely reflects a combination of incomplete lateral thermal equilibration and the rate at which the sample exchanges heat with its surroundings, without assuming a spatially uniform substrate temperature. The thickness-based Biot number, $Bi = h_{tot} L_c / k$, is calculated below. Given the geometry and assembly during the tests, heat loss occurred due to convection and radiation through the upper and bottom faces, so the general characteristic length $L_c = L_{sub}/2 \approx 5 \cdot 10^{-4}$ m (i.e., volume over heat-loss surface area). For an oxide-glass surface with $\varepsilon \approx 0.9$ and near room temperature, $h_{rad} \approx 4\varepsilon\sigma T^3 \approx 5.5$ W/(m^{2}K), so the radiative contribution is comparable in magnitude to typical natural-convection coefficients, and it is not negligible. Then, considering $\rho = 2200$ kg/m^3, $c_p = 740$ J/(kgK), $k = 1.4$ W/(mK), plausible natural-convection coefficients, and $h_{tot} = h_{conv} + h_{rad}$:

Table A1. Biot number estimates.

h_{conv} [W/(m^{2}K)]	h_{total} [W/(m^{2}K)]	Bi [–]
10	15.5	0.006
20	25.5	0.009
40	45.5	0.016

The thickness-based Biot number is small throughout the range considered. However, Figure 7 shows lateral temperature gradients, consistent with the comparable timescale of in-plane diffusion. So, although the Biot criterion appears satisfied, it does not guarantee by itself spatial uniformity. Then, as a plausibility check, considering the energy balance solution as $T(t) = T_\infty + (T_0 - T_\infty) e^{-\frac{t}{\tau_{lumped}}}$, where $\tau_{lumped} = \frac{\rho c_p L_c}{h_{tot}}$, 17.9 s < τ_{lumped} < 52.5 s falls in the same order of magnitude as the observed 20–40 s transient for physically reasonable h_{conv}.

Finally, this thermal-transport mechanisms analysis does not affect the central experimental observation, i.e., the measured $\Delta T(t)$ curves are directly comparable across BG2, BG4, BG6, and the bare substrate regardless of which transport process ultimately limits the transient.

References

1. Thomas, N.G.; Junior, F.G.d.S.; Ninan, N.; Anil, S.; Raju, R.S.; Varghese, N.; Chopra, A.; Thomas, S. Bioglass in Dentistry: A Comprehensive Review of Current Applications and Innovative Frontiers. *J. Dent.* **2025**, *162*, 106017. [CrossRef] [PubMed]
2. Pawar, V.; Shinde, V. Bioglass and Hybrid Bioactive Material: A Review on the Fabrication, Therapeutic Potential and Applications in Wound Healing. *Hybrid Adv.* **2024**, *6*, 100196. [CrossRef]

3. Maximov, M.V.; Maximov, O.C.; Motelica, L.; Ficai, D.; Oprea, O.C.; Trușcă, R.D.; Balahura (Stămat), L.-R.; Pericleanu, R.; Dumbravă, A.Ș.; Corbu, V.M.; et al. Comprehensive Evaluation of 45S5 Bioactive Glass Doped with Samarium: From Synthesis and Physical Properties to Biocompatibility and Antimicrobial Activity. *Coatings* **2025**, *15*, 404. [CrossRef]
4. Safaee, S.; Moghanian, A.; Nesabi, M.; Abe, S.; Harada, K.; Okazaki, H.; Yoshida, K.; Kizilkurtlu, A.A.; Watanabe, I.; Murata, H. Bioactive Glass Coatings for Dental and Maxillofacial Implants: Advanced Deposition Methods to Enhance Bioactivity and Mechanical Strength. *Prog. Org. Coat.* **2026**, *214*, 110021. [CrossRef]
5. Zheng, K.; Niu, W.; Lei, B.; Boccaccini, A.R. Immunomodulatory Bioactive Glasses for Tissue Regeneration. *Acta Biomater.* **2021**, *133*, 168–186. [CrossRef] [PubMed]
6. Jairam, L.S.; Bhaduri, N.; Greeshma, C.; Reddy, K.R. Bioactive Glass Nanoparticles in Dentistry. In *Applications of Nanomaterials in Dentistry*; Elsevier: Amsterdam, The Netherlands, 2026; pp. 339–351.
7. Liang, J.; Lu, X.; Zheng, X.; Li, Y.R.; Geng, X.; Sun, K.; Cai, H.; Jia, Q.; Jiang, H.B.; Liu, K. Modification of Titanium Orthopedic Implants with Bioactive Glass: A Systematic Review of In Vivo and In Vitro Studies. *Front. Bioeng. Biotechnol.* **2023**, *11*, 1269223. [CrossRef] [PubMed]
8. Haddadi, M.H.; Karamian, E.; Bakhsheshi-Rad, H.R.; Kasiri-Asgarani, M. Investigation of the Effect of Bioglass-58S Content on Structural and Biological Properties of PCL-Chitosan-58S-Bioactive Glass Composite Coating for Bone Tissue Engineering Application. *Ceram. Int.* **2023**, *49*, 8190–8195. [CrossRef]
9. Stan, G.E.; Montazerian, M.; Shearer, A.; Stuart, B.W.; Baino, F.; Mauro, J.C.; Ferreira, J.M.F. Critical Advances in the Field of Magnetron Sputtered Bioactive Glass Thin-Films: An Analytical Review. *Appl. Surf. Sci.* **2024**, *646*, 158760. [CrossRef]
10. Shaaban, K.S.; Alyousef, H.A.; Alotaibi, B.M.; El-Rehim, A.F.A.; Wahab, E.A.A. The Vital Role of TiO_2 on the Bioglass System P_2O_5-CaO-B_2O_3-SiO_2-K_2O for Optics and Shielding Characteristics. *J. Inorg. Organomet. Polym. Mater.* **2022**, *32*, 4295–4303. [CrossRef]
11. Wu, X.; Guo, Q. Bioresorbable Photonics: Materials, Devices and Applications. *Photonics* **2021**, *8*, 235. [CrossRef]
12. Hambitzer, L.; Hornbostel, J.M.; Roolfs, L.; Prediger, R.; Kluck, S.; Zheng, K.; Lee-Thedieck, C.; Kotz-Helmer, F. Bioactive Glass Microscaffolds Fabricated by Two-Photon Lithography. *Adv. Mater.* **2025**, *37*, 2504475. [CrossRef] [PubMed]
13. Baranowska, A.; Kochanowicz, M.; Wajda, A.; Leśniak, M.; Żmojda, J.M.; Miluski, P.; Zgłobicka, I.; Kurzydłowski, K.J.; Dorosz, D. Luminescence Sensing Method for Degradation Analysis of Bioactive Glass Fibers. *Sensors* **2021**, *21*, 2054. [CrossRef] [PubMed]
14. Ma, L.; Zhou, Y.; Zhang, Z.; Liu, Y.; Zhai, D.; Zhuang, H.; Li, Q.; Yuye, J.; Wu, C.; Chang, J. Multifunctional Bioactive Nd-Ca-Si Glasses for Fluorescence Thermometry, Photothermal Therapy, and Burn Tissue Repair. *Sci. Adv.* **2020**, *6*, 32. [CrossRef] [PubMed]
15. Du, J.; Ding, H.; Fu, S.; Li, D.; Yu, B. Bismuth-Coated 80S15C Bioactive Glass Scaffolds for Photothermal Antitumor Therapy and Bone Regeneration. *Front. Bioeng. Biotechnol.* **2023**, *10*, 1098923. [CrossRef] [PubMed]
16. Bednarski, H.; Hajduk, B. Dispersion of Thermo-Optic Coefficient of Optical Polymers. *Polymer* **2021**, *230*, 124074. [CrossRef]
17. Ali, R.; Saleem, M.; Pääkkönen, P.; Honkanen, S. Thermo-Optical Properties of Thin-Film TiO_2–Al_2O_3 Bilayers Fabricated by Atomic Layer Deposition. *Nanomaterials* **2015**, *5*, 792–803. [CrossRef]
18. Jaglarz, J.; Dulian, P.; Karasiński, P. Thermo-Optical Properties of Porous Silica Thin Films Produced by Sol-Gel Method. *Mater. Chem. Phys.* **2020**, *243*, 122603. [CrossRef]
19. Moretti, L.; De Stefano, L.; Rossi, A.M.; Rendina, I. Dispersion of Thermo-Optic Coefficient in Porous Silicon Layers of Different Porosities. *Appl. Phys. Lett.* **2005**, *86*, 061107. [CrossRef]
20. Shoji, I.; Sato, Y.; Kurimura, S.; Lupei, V.; Taira, T.; Ikesue, A.; Yoshida, K. Thermal-Birefringence-Induced Depolarization in Nd:YAG Ceramics. *Opt. Lett.* **2002**, *27*, 234. [CrossRef] [PubMed]
21. Zi, Y.; Cun, Y.; Bai, X.; Xu, Z.; Haider, A.A.; Qiu, J.; Song, Z.; Huang, A.; Zhu, J.; Yang, Z. Negative Lattice Expansion-Induced Upconversion Luminescence Thermal Enhancement in Novel Na_2MoO_4:Yb^{3+}, Er^{3+} Transparent Glass Ceramics for Temperature Sensing Applications. *J. Mater. Chem. C.* **2023**, *11*, 1541–1549. [CrossRef]
22. Li, L.; Wu, Z.; Lv, P.; Wang, C.; Han, X.; Yang, Y. Persistent Visible Luminescence of SrF_2:Pr^{3+} for Ratiometric Thermometry. *Opt. Express* **2022**, *30*, 31889. [CrossRef] [PubMed]
23. Fotu, M.; Nicoară, A.I.; Manolache, Ș.; Bacalum, M.; Moisa, R.; Trușcă, R.D.; Isopencu, G.O.; Busuioc, C. Bioceramics Based on Li-Modified Bioactive Glasses for Bone Tissue Regeneration. *Materials* **2026**, *19*, 153. [CrossRef] [PubMed]
24. de Souza, J.R.; Kukulka, E.C.; Araújo, J.C.R.; Campos, T.M.B.; do Prado, R.F.; de Vasconcellos, L.M.R.; Thin, G.P.; Borges, A.L.S. Electrospun Polylactic Acid Scaffolds with Strontium- and Cobalt-doped Bioglass for Potential Use in Bone Tissue Engineering Applications. *J. Biomed. Mater. Res. B Appl. Biomater.* **2023**, *111*, 151–160. [CrossRef] [PubMed]
25. Kotrbová, L.; Uhlířová, T.; Pabst, W.; Hubálková, J.; Kotouček, M. Thermal Conductivity of Silica Refractories and Its Temperature Dependence during Thermal Cycling, Compared to Silicite and Sandstone. *Open Ceram.* **2025**, *21*, 100735. [CrossRef]
26. Bajda, S.; Liu, Y.; Tosi, R.; Cholewa-Kowalska, K.; Krzyzanowski, M.; Dziadek, M.; Kopyscianski, M.; Dymek, S.; Polyakov, A.V.; Semenova, I.P.; et al. Laser Cladding of Bioactive Glass Coating on Pure Titanium Substrate with Highly Refined Grain Structure. *J. Mech. Behav. Biomed. Mater.* **2021**, *119*, 104519. [CrossRef] [PubMed]

27. Lozano, Y.; Levy, D.; Salazar-Bloise, F. Polarization-Resolved Speckle Technique for Rapid Non-Destructive Characterization of Macroporous Silica Thin Films. *Sensors* **2026**, *26*, 1431. [CrossRef] [PubMed]
28. Jaglarz, J.; Dulian, P.; Karasiński, P.; Winkowski, P. Scattering Phenomena in Porous Sol-Gel-Derived Silica Films. *Coatings* **2020**, *10*, 509. [CrossRef]
29. Garahan, A.; Pilon, L.; Yin, J.; Saxena, I. Effective Optical Properties of Absorbing Nanoporous and Nanocomposite Thin Films. *J. Appl. Phys.* **2007**, *101*, 014320. [CrossRef]
30. Pfiester, N.A.; Grossklaus, K.A.; Stevens, M.A.; Vandervelde, T.E. Effect of Microstructure on the Optical Properties of Sputtered Iridium Thin Films. *Opt. Mater. Express* **2020**, *10*, 1120. [CrossRef]
31. Navid, A.; Pilon, L. Effect of Polarization and Morphology on the Optical Properties of Absorbing Nanoporous Thin Films. *Thin Solid Films* **2008**, *516*, 4159–4167. [CrossRef]
32. Hossain, M.F.; Chan, H.P.; Uddin, M.A. Simultaneous Measurement of Thermo-Optic and Stress-Optic Coefficients of Polymer Thin Films Using Prism Coupler Technique. *Appl. Opt.* **2010**, *49*, 403. [CrossRef] [PubMed]
33. Xue, X.; Zhang, H.; Liu, H.; Wang, S.; Li, J.; Zhou, Q.; Chen, X.; Ren, X.; Jing, Y.; Deng, Y.; et al. Rational Design of Multi-functional CuS Nanoparticle-PEG Composite Soft Hydrogel-Coated 3D Hard Polycaprolactone Scaffolds for Efficient Bone Regeneration. *Adv. Funct. Mater.* **2022**, *32*, 2202470. [CrossRef]
34. Wang, L.; Long, N.J.; Li, L.; Lu, Y.; Li, M.; Cao, J.; Zhang, Y.; Zhang, Q.; Xu, S.; Yang, Z.; et al. Multi-Functional Bismuth-Doped Bioglasses: Combining Bioactivity and Photothermal Response for Bone Tumor Treatment and Tissue Repair. *Light Sci. Appl.* **2018**, *7*, 1. [CrossRef] [PubMed]
35. Carslaw, H.S.; Jaeger, J.C. *Conduction of Heat in Solids*, 2nd ed.; Oxford University Press: Oxford, UK, 1959.
36. Crank, J. *The Mathematics of Diffusion*, 2nd ed.; Oxford University Press: Oxford, UK, 1975.
37. Incropera, F.P.; DeWitt, D.P.; Bergman, T.L.; Lavine, A.S. *Fundamentals of Heat and Mass Transfer*, 6th ed.; John Wiley & Sons: Hoboken, NJ, USA, 2007.
38. Almond, D.P.; Patel, P.M. *Photothermal Science and Techniques*; Chapman & Hall: London, UK, 1996.

Disclaimer/Publisher's Note: The statements, opinions and data contained in all publications are solely those of the individual author(s) and contributor(s) and not of MDPI and/or the editor(s). MDPI and/or the editor(s) disclaim responsibility for any injury to people or property resulting from any ideas, methods, instructions or products referred to in the content.